

Title:

Dynamic fluctuations in integration and segregation within the human functional connectome

Authors:

James M. Shine^{1,2}, Peter T. Bell³, Oluwasanmi Koyejo¹, Krzysztof J. Gorgolewski¹, Craig A. Moodie¹, and Russell A. Poldrack¹

Affiliations:

1 – Department of Psychology, Stanford University, Stanford, CA, USA

2 – Neuroscience Research Australia, The University of New South Wales, Sydney, NSW, Australia

3 – Queensland Brain Institute, The University of Queensland, Brisbane, QLD, Australia

Corresponding author:

James M. Shine – macshine@stanford.edu

Abstract:

Higher brain function relies upon the ability to flexibly integrate information across specialized communities of macroscopic brain regions, but it is unclear how this mechanism manifests over time. Here we characterized patterns of time-resolved functional connectivity using resting state and task fMRI data from a large cohort of unrelated subjects. Our results demonstrate that dynamic fluctuations in network structure during the resting state transition between states of integrated and segregated network topology. These patterns were altered during task performance, demonstrating a higher level of network integration that tracked with task complexity. Replication analyses demonstrated that the results were reproducible across sessions, sample populations and datasets. Together these results provide evidence for metastability in the brain's coordination between integration and segregation.

Main Text:

A fundamental aspect of higher brain function is the ability to flexibly integrate communication between a range of specialized sub-networks (1, 2). To achieve this dynamic equilibrium, it has been hypothesized that the human brain strikes a metastable balance between the local segregation of function and the global integration of information (3-7). An emerging picture from this recent work suggests that a relatively fixed structural scaffold gives rise to a highly dynamic functional landscape (1, 8, 9), in which the emergence of momentary neural coalitions forms the basis for complex cognitive functions (10), learning (11) and consciousness (12). However, there is currently little direct evidence regarding how this metastable balance is achieved and the manner in which it evolves over time.

Here we capitalize on recent advancements in high-speed fMRI acquisition by analyzing sub-second resolution resting state and task data using a recently-described metric for time-resolved connectivity analysis (13). Our examination of the evolution of network structure over the course of seconds to minutes demonstrates that the human brain traverses a network state space that fluctuates between topological configurations that emphasize either segregation or integration.

We first calculated patterns of time-resolved functional connectivity in a cohort of 92 unrelated subjects obtained from the Human Connectome Project (HCP) (14). We then performed graph theoretical analyses on these data that identified the topological properties of each brain region within each temporal window (15). In order to test whether the results were reflective of statistically significant non-stationary fluctuations in brain connectivity, in accordance with recent work

(16, 17), our results were tested against a stationary null model. Furthermore, all results were replicated in: i) an independent resting state session in these same 92 individuals; ii) a second set of 92 unrelated individuals from the HCP sample, and; iii) a set of 152 individuals obtained from the Nathan Kline Institute (NKI), Rockland sample (18). The results also survived a range of preprocessing approaches, and we exhaustively tested and rejected any relation of the results to head motion, which is a concern in resting state fMRI (19) (see *Supplementary Materials*).

To characterize time-resolved network topology, we computed region \times region time-resolved functional connectivity matrices using the Multiplication of Temporal Derivatives (MTD) (13) within a sliding temporal window of 10 seconds (see *Supplementary Materials*) (Figure S1). We then performed community detection within each window, which enabled classification of each region according to its profile of within- (W_T) and between-module (B_T) connectivity (Figure S2 and *Supplementary Materials*). Consistent with previous work, we subsequently classified the information processing role of each region within each temporal window based on its' cartographic class (15, 20, 21) (See Figure 1b for details of classification). For instance, a region with high W_T and B_T was classified as a 'connector hub' and by inference, was considered to promote global integration (Figure 1b), whereas a region with high W_T but low B_T was classified a 'provincial hub' and was considered to promote within-module integration. We found that a different class of regions, peripheral nodes, which have relatively weak connectivity both within and between modules, dominated the cartographic landscape (Figure 1d), suggesting that the majority of regions were topologically isolated over time, with a minority of connector hub regions providing a functional bridge between otherwise isolated neural communities

(see Figure 1c). Importantly, the pattern of cartographic classes within the resting brain was significantly different from the pattern observed in the stationary null model based on the mean covariance structure of the data ($F_{1,91} = 310$, $p < 0.001$), rejecting the null hypothesis of stationary network cartography (Figure 1d) and suggesting that the functional connectome explores a dynamical repertoire that plays out over seconds to minutes in the resting brain.

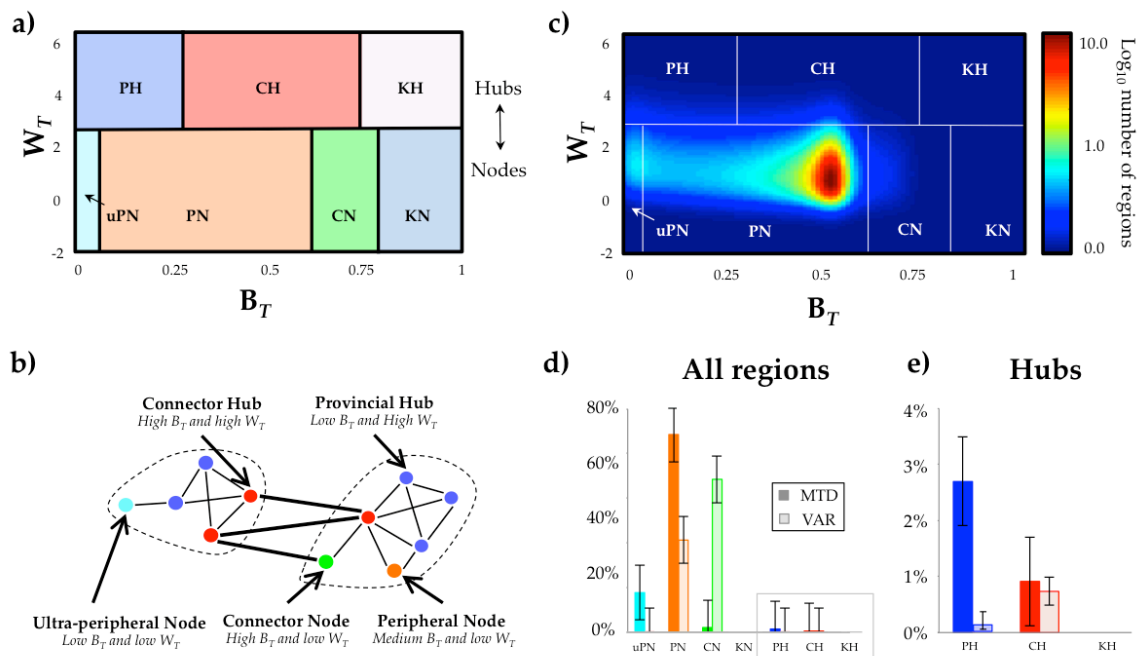


Figure 1: Dynamic Cartographic Analysis. a) Regions were classified according to within- (W_T) and between-module (B_T) connectivity: hub regions ($W_T \geq 2.5$) were parcellated into provincial ($B_T < 0.3$), connector ($0.3 \leq B_T < 0.8$) or kinless hubs ($B_T \geq 0.8$); nodes ($W_T < 2.5$) were parcellated into ultra-peripheral ($B_T < 0.05$), peripheral ($0.05 \leq B_T < 0.6$), connector ($0.6 \leq B_T < 0.85$) and kinless nodes ($B_T \geq 0.85$), in line with (15); b) schematic diagram of each cartographic class – kinless nodes and kinless hubs are not shown, as they were not found in any temporal window for any subject in our analysis; c) group mean joint histogram of W_T and B_T during rest – intensity in each 100×100 cell reflects the \log_{10} frequency that each cell was occupied during the resting state session; d) mean percentage of each time-series associated with each cartographic class for resting state data (dark) and VAR null data (light) – resting data was associated with a higher proportion

of ultra-peripheral ($W_T < 2.5$ & $B_T < 0.05$) and peripheral nodes ($W_T < 2.5$ & $B_T < 0.30$) than the VAR null data (mixture of peripheral and connector nodes) – error bars reflect standard deviation of region frequency over 92 unrelated subjects; e) mean percentage of each time-series associated with each hub class. Abbreviations: uPN – ultra-peripheral nodes; PN – peripheral nodes (orange); CN – connector nodes (green); PH – peripheral hubs (dark blue) and CH – connector hubs (red); KN – kinless nodes (sky blue); KH – kinless hubs (tan); VAR – vector autoregressive null model.

We also observed distinct and reproducible patterns of network hub topology in the time-resolved resting brain. The relative percentage of time that each region behaved as each cartographic class demonstrated significant heterogeneity (see Figure 2 and S3). For example, frontoparietal, striatal and hippocampal regions spending the greatest duration of time as connector hubs (Figure 2a), implicating these regions as important for facilitating whole-brain integration. In contrast, regions classically associated with the default and cinguloparietal systems were the most likely to act as provincial hubs over time, thus promoting communication within their own module (Figure 2b & c).

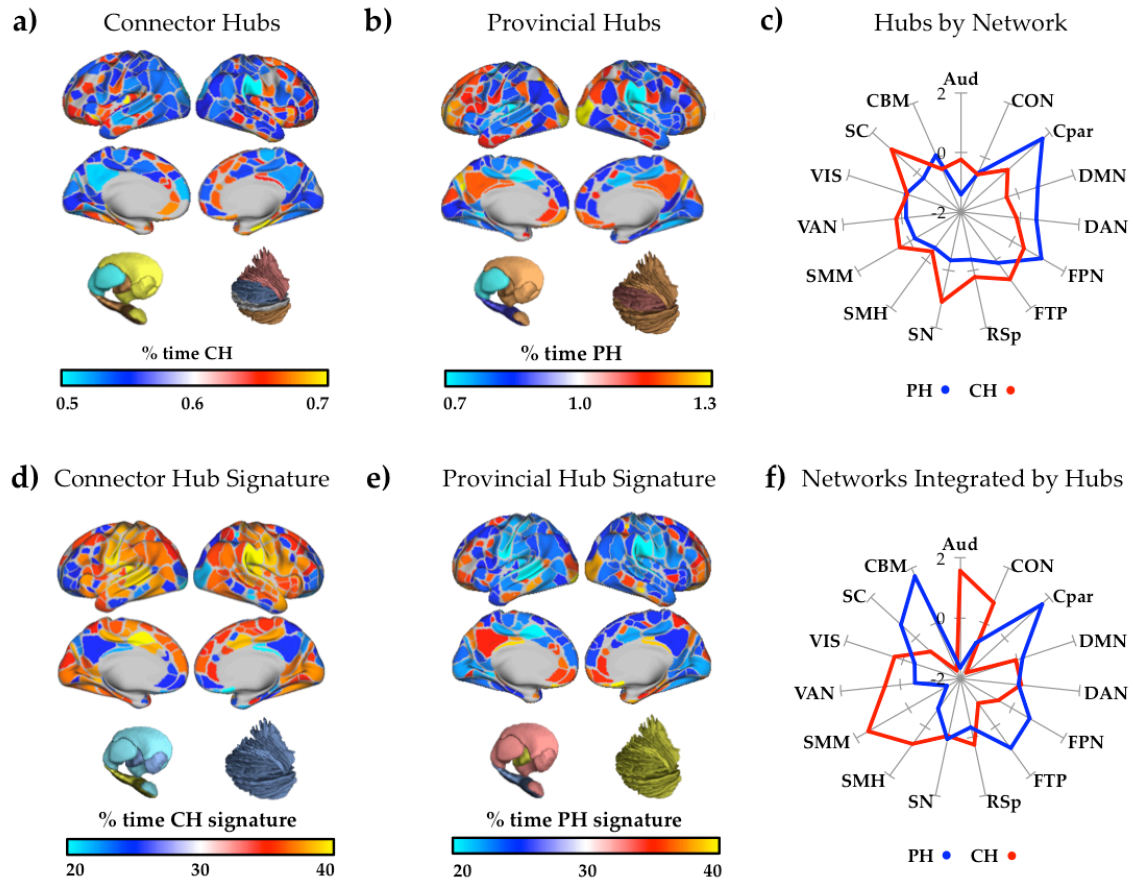


Figure 2: Dynamic Hub Structure in the Resting Brain. a) The regional pattern associated with regions that spent the highest proportion of the resting state session acting as a connector hub (red/yellow), with respect to all other regions; b) regional pattern associated with preferential increase in time acting as a provincial hub (red/yellow), with respect to all other regions; c) Z-scored mean percentage of time acting as either a connector or provincial hub, collapsed into each of 15 pre-defined large-scale cortical networks (31); d) the regional pattern associated with regions that spent the most time within the same module as a connector hub (red/yellow), with respect to all other regions; e) the regional pattern associated with preferential increase in time occurring within the same module as a provincial hub (red/yellow), with respect to all other regions; f) Z-scored mean percentage of time within the same module as a connector or provincial hub, collapsed into each of 15 pre-defined brain systems defined in a previous time-averaged study (35). Images available at <http://neurovault.org/collections/HAWDIOCD/>. Key: Aud – Auditory; CON – Cingulo-Opercular; Cpar – Cingulo-parietal; DMN – Default Mode; DAN – Dorsal Attention; FPN – Frontoparietal; FTP – Fronto-temporal; RSp – Retrosplenial; SN –

Salience; SMH – Somatomotor Hand; SMM – Somatomotor Mouth; VAN – Ventral Attention; VIS – Visual; SC – Subcortical; CBM – Cerebellum.

Although the most integrated regions within a complex network are crucial for defining the information processing capacity of the system, their functional importance is defined by which nodes they inter-connect (6). By identifying the regions that were within the same module as a connector hub (and hence, were integrated within that window), we found that the connector hubs preferentially integrated primary processing regions, such as visual, auditory and somatomotor cortex. In contrast, provincial hubs primarily connected with regions within the cerebellum and cinguloparietal network (Figure 2f). These results suggest that the integrative core of the brain over time was composed of dynamic and flexible hubs that recruited the involvement of neuronal assemblies composed of relatively segregated nodes.

An analysis of temporal fluctuations in cartography identified the presence of two topological ‘states’ that alternated over time, one of which was characterized by the predominance of ultra-peripheral nodes and provincial hubs (reflecting relatively segregated network function; segregation Z-score [Z_s] ≥ 1.65 : $14.90 \pm 1.8\%$ of time series across subjects), and another that was characterized by the predominance of connector hubs, connector nodes and peripheral nodes (reflecting relatively integrated network function; integration Z-score [Z_i] ≥ 1.65 : $29.26 \pm 3.7\%$ of time series) (Figure 3a). The majority of the resting session was associated with a mixture of these two states (both Z_i and $Z_s < 1.65$: $55.79 \pm 5.1\%$ of time series), providing evidence for metastable dynamics in the resting brain (7). The more integrated state was characterized by connectivity between default/frontoparietal systems and primary processing networks, such as the

auditory, somatosensory and visual networks (Figure S4; FDR $p < 0.05$). In contrast, the segregated state demonstrated stronger internal connectivity within the default and frontoparietal systems, which became functionally detached from the primary processing systems (Figure S4; FDR $p < 0.05$). These results suggest that the brain had to disengage the connections between higher-level control systems and primary processing systems to enter into the more segregated state. The two states also showed a tradeoff in their topology, such that temporal windows associated with the segregated state had significantly greater modularity ($Q_s = 0.55 \pm 0.1$ *vs.* $Q_I = 0.42 \pm 0.2$; $p < 0.001$) whereas those associated with the integrated state had greater global efficiency ($E_s = 0.18 \pm 0.03$ *vs.* $E_I = 0.24 \pm 0.05$; $p < 0.001$; Figure 3d). This topological double dissociation suggests that the dynamic fluctuations in network structure constrain global information processing. Furthermore, these patterns were absent in the VAR null dataset (Figure S6).

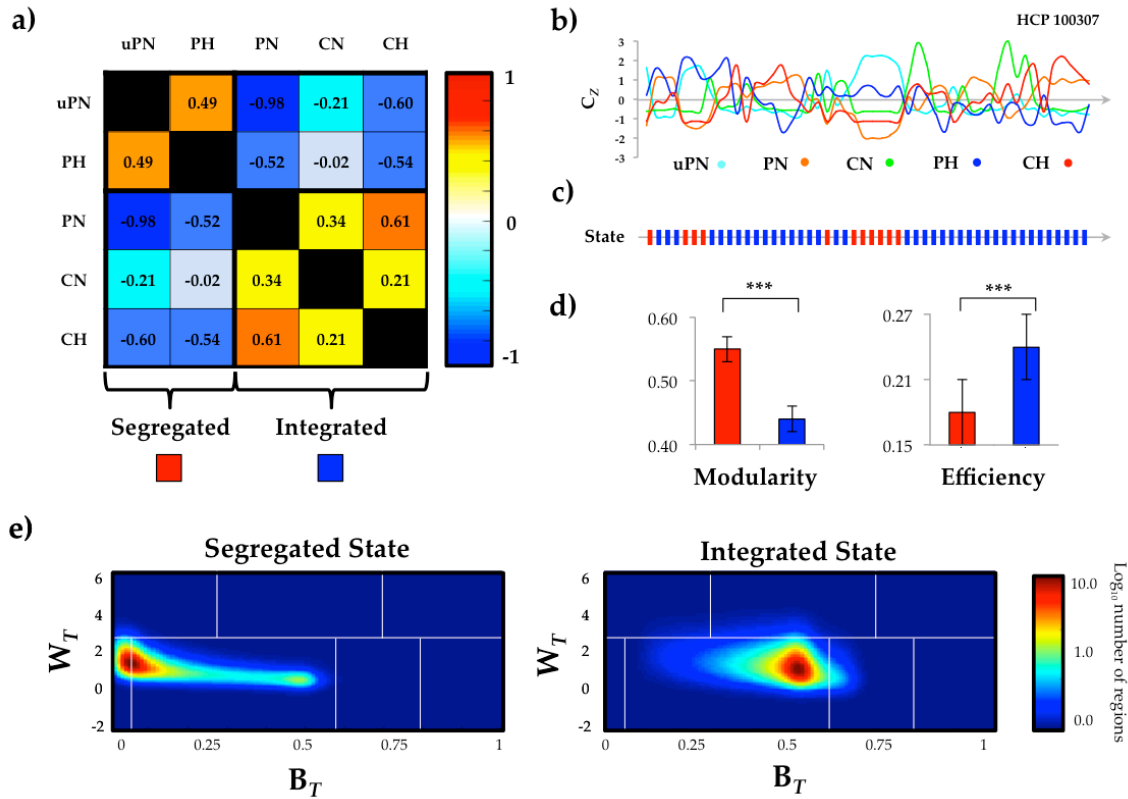


Figure 3: Dynamic Cooperation and Competition between Cartographic Classes: a) Temporal fluctuations in network topology identified the presence of two temporal topological ‘states’: one composed of ultra-peripheral nodes and peripheral hubs (‘Segregated’); and the other composed of peripheral nodes, connector nodes and connector hubs (‘Integrated’); b) a characteristic time series (subject ID: HCP 100307) of the relative proportion of regions associated with each cartographic class (colored lines above); c) cartographic time series were then parcellated according to each state (Segregated [red] – prevalence of uPN and PH; Integrated [blue] – prevalence of PN, CN and CH); d) temporal windows associated with the segregated state were associated with significantly greater modularity and reduced global efficiency than those associated with the integrated state; e) a k-means ($k = 2$) clustering analysis using on the time-resolved joint histogram confirmed the presence of these two states in the cartographic profile analysis. Key: uPN – ultra-peripheral nodes; PN – peripheral nodes; CN – connector nodes; PH – peripheral hubs; CH – connector hubs; *** - significant at $p < 0.001$.

In order to assess the temporal classification into two states without requiring the labeling of each node into cartographic classes (15), for each window we computed a joint histogram of within- and between-module connectivity measures, which we refer to here as a “cartographic profile”. K-means clustering of these full profiles ($k = 2$, although the results were stable for $k > 2$; see *Supplementary Methods*) confirmed the identification of relatively integrated and segregated states described above (Z_s and $Z_I > 0$; Dice’s coefficient between analyses = 0.792 ± 0.04 ; Figure 3e), providing further evidence that the brain fluctuates between states with distinct topologies, and by inference, different modes of information processing (see Figure 3e). Examination of individual subject data confirmed that the resting brain explored a dynamical repertoire within the topological space, fluctuating between the integrated and segregated temporal states identified in the clustering analysis above (see Figure S10 & S11).

A direct prediction of our findings from the time-resolved resting analysis is that the balance between network integration and segregation of the brain should track ongoing cognitive function over time. We tested this hypothesis using data from two tasks from the HCP (22) in the discovery cohort of 92 subjects: a simple motor task and a visual N-back task. We observed a distinct alteration in the cartographic profile during the performance of both tasks when compared to the resting state (Figures 4a & b), with a significant increase in connectivity between modules (Figure 4b), suggesting that the brain had entered into a state of higher integration in order to meet the demands of the task (Motor: $F_{1,91} = 392.1$, $p < 0.001$; N-back: $F_{1,91} = 420.3$, $p < 0.001$; Figures 4c). Importantly, the extent of reconfiguration during task performance varied as a function of the cognitive demands of the task, with the N-back task showing a greater shift towards a more integrated network topology (Figure 4d). We quantified this effect by

estimating the affine transformation required to align each subjects' resting cartographic profile with their profile during task. This analysis demonstrated that the N-back task caused a shift towards a more integrated network topology relative to the Motor task (transformation along the B_T axis – N-back: +0.21; Motor: +0.18; $t_{91} = 5.18$, $p < 0.001$; Figure 4d).

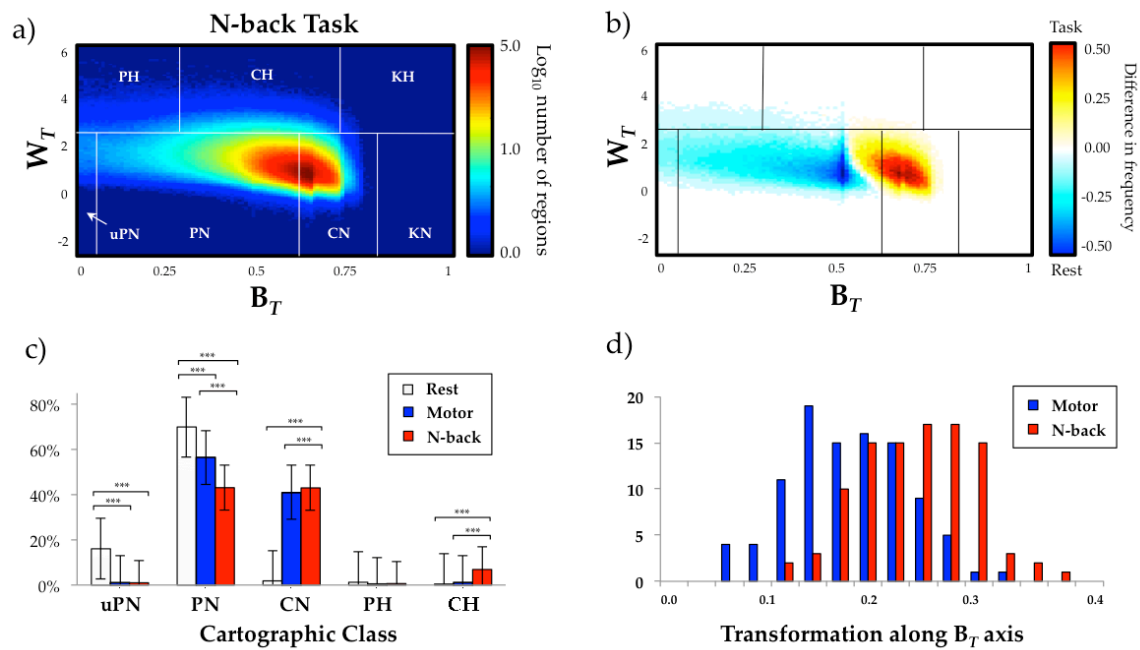


Figure 4: Alteration of cartographic profile during task performance: a) group mean joint histogram of W_T and B_T for task blocks during the N-back task – intensity in each 100×100 cell reflects the log_{10} frequency that each cell was occupied during the resting state session; b) regions of the 2-dimensional joint histogram space that were significantly different between N-back task blocks and the resting state (paired-samples t-test) – colored points indicate a region that survived false discovery correction ($q < 0.01$): yellow/red – increased frequency during N-back task blocks; blue/light blue – increased frequency during resting state; c) mean percentage of each time-series associated with each cartographic class for resting state data (grey), motor task (blue) and N-back task blocks (red) – resting data was associated with a higher proportion of ultra-peripheral ($W_T < 2.5$ & $B_T < 0.05$) and peripheral nodes ($W_T < 2.5$ & $B_T < 0.30$) than both sets of task data, which shifted to a more integrated state as a function of task complexity – error bars reflect standard deviation of region frequency over 92 unrelated subjects; d) histogram reflecting the

affine transformation required to match each participants' resting state cartographic profile to match the cartographic profile during the each task along the between-module (B_T) connectivity axis (Motor – blue; N-back – red). Abbreviations: uPN – ultra-peripheral nodes; PN – peripheral nodes (dark blue); CN – connector nodes (green); PH – peripheral hubs (orange) and CH – connector hubs (red).

Notably, participants spent less time in the segregated state during performance of the two tasks than during rest ($Z_s > 1.65$ – Motor: $6.57 \pm 1.9\%$; N-back: $6.30 \pm 1.5\%$); however, we found that the cartographic profile preferentially shifted towards the more segregated state during the interleaved 'rest' blocks during both tasks (Motor: $68.42 \pm 2.3\%$ of rest TRs were associated with $Z_s > 1.65$; N-back: $61.63 \pm 1.4\%$; see Figure S12). In addition, both tasks showed an increase in global efficiency ($r_{Mot.E}$: 0.354 ± 0.03 ; $r_{Nback.E}$: 0.340 ± 0.04) and a decrease in modularity ($r_{Mot.Q}$: -0.312 ± 0.02 ; $r_{Nback.Q}$: -0.333 ± 0.05) as a function of task, further implicating the need to flexibly trade-off global topological properties in order to complete the behavioral tasks (23). Together, these results suggest that the performance of a demanding cognitive task caused a targeted reorganization of the integrative core of the brain into a unique network assembly that was integral for the performance of each task (24).

To test the reliability of our results, we performed three separate replication analyses: i) on a second resting state session (with identical imaging parameters) from the same cohort of 92 unrelated subjects; ii) on a different cohort of 92 unrelated subjects (with identical imaging parameters) from the HCP consortium; and iii) on 152 subjects from a separate dataset acquired at a different scanning site, acquired using high-resolution functional data from the NKI Rockland dataset (18). In each case, we replicated the analyses described

above on each subject and then summarized each outcome measure of interest at the group level. We then compared the results obtained from the replication with the results obtained from the original sample using a parcel-wise Pearson's correlation coefficient. For each analysis, we observed strong positive correlations between the summary measures derived from each analysis (minimum $r = 0.564$; all $p < 0.0001$; see *Supplementary Materials*), suggesting that the time-resolved measures identified in this study were reliable across sessions, individuals and even across datasets collected using different scanners and imaging protocols.

In this study, we mapped the spatiotemporal dynamics of network structure in the human brain, revealing a dynamical system that fluctuates between segregated and integrated network topology. Our results thus provide evidence for metastable dynamics in the human brain (Figure 3). In the resting state, coordinated fluctuations in network structure supported the emergence of transient neural coalitions that were integrated by a network of regions comprising frontal, parietal and temporal cortex, as well as striatum (Figure 2). In contrast, the cartographic profile of the brain was modulated by the performance of both a simple motor and more cognitively-demanding task, both of which caused a targeted reorganization of network architecture into a highly integrated neuronal assembly that varied as a function of task complexity (Figure 4).

Our results demonstrate that the functional neural landscape spontaneously transitions between coordinated assemblies of node classes that comprise one state of high modularity and low global efficiency and another contrasting topological state of reduced modularity and higher global efficiency (Figure 3). Interestingly, the most preferentially segregated regions in the brain (i.e. regions

in sensory and motor cortices) were the most likely to be 'recruited' by the most integrated regions (i.e. frontal, parietal and temporal cortex, as well as striatum) (Figure 2f). Together with the fluctuations observed at the whole brain level, these findings suggest that the resting brain consists of a dynamically evolving neural architecture, in which a strongly integrated core inter-connects a range of other regions, with the majority of the brain remaining relatively isolated from the core. As such, our results suggest that the patterns observed in time-averaged analyses of the resting brain may be composed of a combination of different signals – those demonstrating baseline levels of communication between relatively segregated regions that closely mirror the structural connectome (9) and those reflective of the functional activity superimposed onto the idling architecture of the brain, such as the patterns tracking the internal cognitive state over time (25). This hypothesis is supported directly by our finding that the global information processing state of the brain was altered during the performance of both a simple motor task, as well as an N-back task that recruits working memory maintenance and updating (Figure 4). It follows that specific departures from the resting spatiotemporal architecture should be observed during the performance of other behavioral tasks, when unique networks of regions should coordinate their activity to promote integration, as well as during slow wave sleep and in the minimally conscious state (26), when the pattern should shift towards a more segregated architecture.

Although the functional implication of the results of our analyses require further confirmation, particularly without an effective means for tracking the contents of conscious thoughts over time, one potential hypothesis is that the areas identified as important for integration in our study reflect the activity of the so-called 'dynamic core' (27, 28). There is already strong empirical support for these

concepts in the neuroscience literature (6), predominantly from global workspace theories of consciousness in which the widespread 'distribution' of information is proposed to mediate conscious experience (2). Indeed, given the known importance of whole-brain integration for the execution of complex behavior (29), the regions integrated by the connector hubs within each window represent an attractive candidate for dynamically tracking the activity within the global workspace. In future studies, the definition of the manner in which distributed neural regions interact with one another across multiple time-scales (30) will help to shift our modern theories of brain function closer to a biological explanation of the neuronal mechanisms that support conscious experience.

Acknowledgements:

The data reported in this paper were made publicly available by the Human Connectome Project and 1000 Functional Connectomes project. There were no conflicts of interest for any authors. JMS, OK, PTB and RAP designed the analysis. JMS performed the analysis and wrote the first draft. JMS, OK, CAM, PTB, KJG and RAP reviewed and edited the manuscript. We would like to thank Vanessa Sochat for her assistance with the implementation of the analysis, Michael Riis and Ian Eisenberg for their helpful insights and Tim Laumann, Claire O'Callaghan, Patrick Bissett and Rav Suri for their critical review of the manuscript.

References:

1. S. E. Petersen, O. Sporns, Brain Networks and Cognitive Architectures. *Neuron*. **88**, 207–219 (2015).
2. S. Dehaene, J. P. Changeux, L. Naccache, Conscious, preconscious, and subliminal processing: a testable taxonomy. *Trends in Cognitive Sciences*. **10**, 204–211 (2006).
3. G. Tononi, O. Sporns, A measure for brain complexity: relating functional segregation and integration in the nervous system. *Proceedings of the National Academy of Sciences*. **91**, 5033–5037 (1994).
4. M. P. van den Heuvel, O. Sporns, Network hubs in the human brain. *Trends in Cognitive Sciences*. **17**, 683–696 (2013).
5. O. Sporns, Network attributes for segregation and integration in the human brain. *Current Opinion in Neurobiology*. **23**, 162–171 (2013).
6. F. Varela, J. P. Lachaux, E. Rodriguez, The brainweb: phase synchronization and large-scale integration. *Nature Reviews Neuroscience*. **2**, 229–239 (2001).
7. J. Kelso, Multistability and metastability: understanding dynamic coordination in the brain. *Transactions of the Royal Society B*. **367**, 906–918 (2012).
8. G. Deco, G. Tononi, M. Boly, M. L. Kringelbach, Rethinking segregation and integration: contributions of whole-brain modelling. *Nat. Rev. Neurosci.* **16**, 430–439 (2015).
9. K. Shen, R. M. Hutchison, G. Bezgin, S. Everling, A. R. McIntosh, Network structure shapes spontaneous functional connectivity dynamics. *J. Neurosci.* **35**, 5579–5588 (2015).
10. M. W. Cole, D. S. Bassett, J. D. Power, T. S. Braver, S. E. Petersen, Intrinsic and task-evoked network architectures of the human brain. *Neuron*. **83**, 238–251 (2014).
11. D. S. Bassett, M. Yang, N. F. Wymbs, S. T. Grafton, Learning-induced autonomy of sensorimotor systems. *Nat Neurosci.* **18**, 744–751 (2015).
12. P. Barttfeld *et al.*, Signature of consciousness in the dynamics of resting

- state brain activity. *Proceedings of the National Academy of Sciences*. **112**, 887–892 (2015).
13. J. M. Shine *et al.*, Estimation of dynamic functional connectivity using Multiplication of Temporal Derivatives. *NeuroImage*. **122**, 399–407 (2015).
 14. S. M. Smith *et al.*, Resting state fMRI in the Human Connectome Project. *NeuroImage*. **80**, 144–168 (2013).
 15. R. Guimerà, L. A. Nunes Amaral, Functional cartography of complex metabolic networks. *Nature*. **433**, 895–900 (2005).
 16. A. Zalesky, A. Fornito, L. Cocchi, L. L. Gollo, M. Breakspear, Time-resolved resting state brain networks. *Proceedings of the National Academy of Sciences*. **111**, 10341–10346 (2014).
 17. F. de Pasquale, S. Della Penna, O. Sporns, G. L. Romani, M. Corbetta, A Dynamic Core Network and Global Efficiency in the Resting Human Brain. *Cereb. Cortex*, bhv185 (2015).
 18. K. B. Nooner *et al.*, The NKI-Rockland Sample: A Model for Accelerating the Pace of Discovery Science in Psychiatry. *Front. Neurosci.* **6**, 152 (2012).
 19. J. D. Power, K. A. Barnes, A. Z. Snyder, B. L. Schlaggar, S. E. Petersen, Spurious but systematic correlations in functional connectivity MRI networks arise from subject motion. *NeuroImage*. **59**, 2142–2154 (2012).
 20. O. Sporns, Cerebral cartography and connectomics. *Philos. Trans. R. Soc. Lond., B, Biol. Sci.* **370**, 20140173–20140173 (2015).
 21. O. Sporns, R. F. Betzel, Modular Brain Networks. *Annu Rev Psychol.* **67**, annurev-psych-122414-033634 (2015).
 22. D. M. Barch *et al.*, Function in the human connectome: task-fMRI and individual differences in behavior. *NeuroImage*. **80**, 169–189 (2013).
 23. B. Mišić, O. Sporns, A. R. McIntosh, Communication efficiency and congestion of signal traffic in large-scale brain networks. *PLoS Comput. Biol.* **10**, e1003427 (2014).
 24. F. M. Krienen, B. T. T. Yeo, R. L. Buckner, Reconfigurable task-dependent functional coupling modes cluster around a core functional architecture. *Philos. Trans. R. Soc. Lond., B, Biol. Sci.* **369**, 20130526–20130526 (2014).

25. M. G. Berman *et al.*, Does resting state connectivity reflect depressive rumination? A tale of two analyses. *NeuroImage*. **103**, 267–279 (2014).
26. A. Demertzi *et al.*, Intrinsic functional connectivity differentiates minimally conscious from unresponsive patients. *Brain*. **138**, 2619–2631 (2015).
27. G. Tononi, G. M. Edelman, Consciousness and complexity. *Science*. **282**, 1846–1851 (1998).
28. G. M. Edelman, Naturalizing consciousness: a theoretical framework. *Proceedings of the National Academy of Sciences*. **100**, 5520–5524 (2003).
29. M. P. van den Heuvel, O. Sporns, An anatomical substrate for integration among functional networks in human cortex. *J. Neurosci*. **33**, 14489–14500 (2013).
30. C. J. Honey *et al.*, Slow cortical dynamics and the accumulation of information over long timescales. *Neuron*. **76**, 423–434 (2012).
31. M. F. Glasser *et al.*, The minimal preprocessing pipelines for the Human Connectome Project. *NeuroImage*. **80**, 105–124 (2013).
32. B. B. Avants, C. L. Epstein, M. Grossman, J. C. Gee, Symmetric diffeomorphic image registration with cross-correlation: evaluating automated labeling of elderly and neurodegenerative brain. *Med Image Anal*. **12**, 26–41 (2008).
33. J. D. Power *et al.*, Methods to detect, characterize, and remove motion artifact in resting state fMRI. *NeuroImage*. **84**, 320–341 (2014).
34. Y. Behzadi, K. Restom, J. Liau, T. T. Liu, A component based noise correction method (CompCor) for BOLD and perfusion based fMRI. *NeuroImage*. **37**, 90–101 (2007).
35. E. M. Gordon *et al.*, Generation and Evaluation of a Cortical Area Parcellation from Resting state Correlations. *Cereb. Cortex*, bhu239 (2014).
36. J. Diedrichsen, J. H. Balsters, J. Flavell, E. Cussans, N. Ramnani, A probabilistic MR atlas of the human cerebellum. *NeuroImage*. **46**, 39–46 (2009).
37. M. E. Raichle, The restless brain. *Brain Connectivity*. **1**, 3–12 (2011).

38. T. E. Nichols, A. P. Holmes, Nonparametric permutation tests for functional neuroimaging: a primer with examples. *Hum Brain Mapp.* **15**, 1–25 (2002).
39. M. Rubinov, O. Sporns, Complex network measures of brain connectivity: Uses and interpretations. *NeuroImage.* **52**, 1059–1069 (2010).
40. J. D. Power, B. L. Schlaggar, C. N. Lessov-Schlaggar, S. E. Petersen, Evidence for hubs in human functional brain networks. *Neuron.* **79**, 798–813 (2013).
41. N. Leonardi, D. Van De Ville, On spurious and real fluctuations of dynamic functional connectivity during rest. *NeuroImage.* **104**, 430–436 (2015).
42. A. Zalesky, M. Breakspear, Towards a statistical test for functional connectivity dynamics. *NeuroImage.* **114**, 466–470 (2015).
43. M. Rosvall, C. T. Bergstrom, Maps of random walks on complex networks reveal community structure. *Proceedings of the National Academy of Sciences.* **105**, 1118–1123 (2008).
44. P. J. Mucha, T. Richardson, K. Macon, M. A. Porter, J.-P. Onnela, Community structure in time-dependent, multiscale, and multiplex networks. *Science.* **328**, 876–878 (2010).

Supplementary Materials

Data acquisition

For the primary discovery analysis, minimally preprocessed resting fMRI data were acquired from 100 unrelated participants from the Human Connectome Project (mean age 29.5 years, 55% female) (31). For each participant, 14 minutes 30 seconds of resting state data were acquired using multiband gradient-echo echoplanar imaging. The following parameters were used for data acquisition: relaxation time (TR) = 720 ms, echo time = 33.1 ms, multiband factor = 8, flip angle = 52 degrees, field of view = 208x180 mm (matrix = 104 x 90), 2x2x2 isotropic voxels with 72 slices, alternated LR/RL phase encoding.

In addition to the discovery analysis, we also performed an extensive series of replication analyses including: i) data from the same participants using resting state data acquired during a second rest scan during the same scanning session; ii) an independent cohort of 100 unrelated participants from the HCP dataset using identical acquisition parameters at the same scanning site; and iii) an out-of-sample replication using data collected from the NKI Rockland sample (TR = 650msec; voxel-size 3mm³) as part of the 1000 Functional Connectomes Project (18).

Data pre-processing

Bias field correction and motion correction (12 linear DOF using FSL's FLIRT) were applied to the HCP resting state data as part of the minimal preprocessing pipeline (31). The first 100 time points were discarded from the data due to the presence of an evoked auditory signal associated with noise in the scanner. Resting state data acquired from the NKI Rockland sample were realigned to correct for head motion and then each participants' functional scans were

registered to both their T1-weighted structural image and then to the MNI152 atlas using boundary based registration (<http://fsl.fmrib.ox.ac.uk/fsl/fslwiki/>) and Advanced Normalization Tools software (32). After co-registration, data were manually inspected and of the 173 original participants, 11 [6.3%] scans were discarded due insufficient coverage of orbitofrontal cortex, temporopolar cortex and/or cerebellum.

Temporal artifacts were identified in each dataset by calculating framewise displacement (FD) from the derivatives of the six rigid-body realignment parameters estimated during standard volume realignment (33), as well as the root mean square change in BOLD signal from volume to volume (DVARs). Frames associated with $FD > 0.5\text{mm}$ or $DVARs > 5\%$ were identified, and participants with greater than 20% of the resting time points exceeding these values were excluded from further analysis (HCP group 1: 8/100; HCP group 2: 8/100; NKI group: 10/162). Due to concerns associated with the alteration of the temporal structure of the images, the data used in the main analysis were not 'scrubbed' (33), however we did explicitly compare the results of our experiment with scrubbed data (missing values were corrected using interpolation) and found strong correspondence between the outcome measures of the two studies (see *Validation*). Following artifact detection, nuisance covariates associated with the 12 linear head movement parameters (and their temporal derivatives), FD, DVARs, and anatomical masks from the cerebral spinal fluid and deep cerebral white matter were regressed from the data using the CompCor strategy (34). Finally, in keeping with previous time-resolved connectivity experiments (11), a temporal band pass filter ($0.071 < f < 0.125$ Hz) was applied to the data (see *Validation*).

Brain parcellation

Following pre-processing, the mean time series was extracted from 375 pre-defined regions-of-interest (ROI). To ensure whole-brain coverage, we extracted: 333 cortical parcels (161 and 162 regions from the left and right hemispheres, respectively) using the Gordon atlas (35), 14 subcortical regions from Harvard-Oxford subcortical atlas (<http://fsl.fmrib.ox.ac.uk/>), and 28 cerebellar regions from the SUI atlas (36) for each participant in the study.

Multiplication of temporal derivatives

To estimate functional connectivity between the 375 ROIs, we used a recently described statistical technique (Multiplication of Temporal Derivatives; MTD – <http://github.com/macshine/coupling/>) (13) that allows greater temporal resolution of time-resolved connectivity in BOLD time series data when compared to the conventional sliding-window Pearson's correlation coefficient (13). The MTD is computed by calculating the point-wise product of temporal derivative of pairwise time series (Equation 1). In order to reduce the contamination of high-frequency noise in the time-resolved connectivity data, the MTD is averaged by calculating the mean value over a temporal window, w (<https://github.com/macshine/coupling/>).

$$MTD_{ijt} = \frac{1}{w} \sum_t^{t+w} \frac{(dt_{it} \times dt_{jt})}{(\sigma_{dt_i} \times \sigma_{dt_j})} \quad [1]$$

Equation 1 – Multiplication of Temporal Derivatives, where for each time point, t , the MTD for the pairwise interaction between region i and j is defined according to equation 1, where dt is the first temporal derivative of the i^{th} or j^{th} time series at time t , σ is the standard deviation of the temporal derivative time

series for region i or j and w is the window length of the simple moving average. This equation can then be calculated over the course of a time series to obtain an estimate of time-resolved connectivity between pairs of regions.

Time-resolved functional connectivity

Time-resolved functional connectivity was calculated between all 375 brain regions using the MTD (13) within a sliding temporal window of 14 time points (10.1 seconds for HCP; 16 time points for NKI data ~ 10.4 seconds). Previous work has shown that, when using the MTD, a window length of 7 time points provides optimal sensitivity and specificity for detecting dynamic changes in functional connectivity structure in simulated time series data (13). To balance these benefits with the need to track changes in slow cortical fluctuations which are hypothesized to fluctuate at ~0.1 Hz (37), we used a temporal window of 14 time points to calculate a simple moving average of the MTD, which allowed for estimates of signals at approximately 0.1 Hz. Individual functional connectivity matrices were calculated within each temporal window, thus generating an unthresholded (that is, signed and weighted) 3D adjacency matrix (region \times region \times time) for each participant (see Figure S1).

Vector autoregressive null model

For each time-resolved outcome measure derived in the above analyses, results were directly compared to data simulated using a series of stationary, multi-dimensional vector autoregressive (VAR) models, which were used to generate surrogate regional time series satisfying the null hypothesis of a linearly correlated, stationary, multivariate stochastic process (see Figure S1). In keeping with Zalesky et al. (16), VAR model order was set at 11, appropriately mimicking the expected temporal signature of the BOLD response in 0.72s TR data. The

mean covariance matrix across all 92 subjects from the discovery group was used to generate 2500 independent null data sets, which allows for the appropriate estimation of the tails of non-parametric distributions (38). These time series were then filtered in a similar fashion to the BOLD data. For each analysis, the maximum statistic was concatenated for each independent simulation and then used to populate a null distribution, against which each outcome measure was compared. Null hypotheses were rejected if the observed test statistic was greater than or less than 2.5% of the most extreme values generated by the 2500 VAR trials. Importantly, by comparing each time-resolved outcome measure with the results from the VAR simulations, we could effectively determine whether or not the time-resolved measures allowed for the rejection of the null hypothesis of temporal stationary (See Figure S1).

Time- resolved community structure

The Louvain modularity algorithm from the Brain Connectivity Toolbox (BCT; (39) was used in combination with the MTD to estimate both time-averaged and time-resolved community structure. The Louvain algorithm iteratively maximizes the modularity statistic, Q , for different community assignments until the maximum possible score of Q has been obtained (see Equation 2). The modularity estimate for a given network is therefore a quantification of the extent to which the network may be subdivided into communities with stronger within-module than between-module connections.

$$Q_T = \frac{1}{v^+} \sum_{ij} (w_{ij}^+ - e_{ij}^+) \delta_{M_i M_j} - \frac{1}{v^+ + v^-} \sum_{ij} (w_{ij}^- - e_{ij}^-) \delta_{M_i M_j} \quad [2]$$

Equation 2 – Louvain modularity algorithm, where v is the total weight of the network (sum of all negative and positive connections), w_{ij} is the weighted and signed connection between regions i and j , e_{ij} is the strength of a connection

divided by the total weight of the network, and δ_{MiMj} is set to 1 when regions are in the same community and 0 otherwise. '+' and '-' superscripts denote all positive and negative connections, respectively.

For each temporal window, the community assignment for each region was assessed 500 times and a consensus partition was identified using a fine-tuning algorithm from the Brain Connectivity Toolbox (BCT, <http://www.brain-connectivity-toolbox.net/>). This then afforded an estimate of both the time-resolved modularity (Q_T) and cluster assignment (C_{iT}) within each temporal window for each participant in the study. All graph theoretical measures were calculated on weighted and signed connectivity matrices, such that no arbitrary thresholding was required (39).

Based on time-resolved community assignments, we estimated within-module connectivity by calculating the time-resolved module-degree Z-score (W_{iT} ; within module strength) for each region in our analysis (Equation 3) (15).

$$W_{iT} = \frac{\kappa_{iT} - \bar{\kappa}_{s_{iT}}}{\sigma_{\kappa_{s_{iT}}}} \quad [3]$$

Equation 3 – Module degree Z-score, W_{iT} , where κ_{iT} is the strength of the connections of region i to other regions in its module s_i at time T , $\bar{\kappa}_{s_{iT}}$ is the average of κ over all the regions in s_i at time T , and $\sigma_{\kappa_{s_{iT}}}$ is the standard deviation of κ in s_i at time T .

Time- resolved hub structure

The participation coefficient, B_T , quantifies the extent to which a region connects across all modules (i.e. between-module strength) and has previously been used

to characterize hubs within brain networks (e.g. see (4, 40)). The B_T for each region was calculated within each temporal window using Equation 4.

$$B_{iT} = 1 - \sum_{s=1} \left(\frac{\kappa_{isT}}{\kappa_{iT}} \right)^2 \quad [4]$$

Equation 4 - Participation coefficient B_{iT} , where κ_{isT} is the strength of the positive connections of region i to regions in module s at time T , and κ_{iT} is the sum of strengths of all positive connections of region i at time T . The participation coefficient of a region is therefore close to 1 if its connections are uniformly distributed among all the modules and 0 if all of its links are within its own module.

Cartographic Analysis

Regions were classified according to their position in a 2-dimensional W_T – B_T parameter space using the delineations suggested by Guimera and Amaral (2005). Specifically, we classified regions with $W_T < 2.5$ as non-hub nodes and regions with $W_T \geq 2.5$ as hubs. Within the class of nodes, regions were further categorized into: ‘ultra-peripheral’ ($B_T < 0.05$), ‘peripheral’ ($0.05 \leq B_T < 0.3$), ‘connector’ ($0.3 \leq B_T < 0.65$) and ‘kinless’ ($B_T \geq 0.65$) nodes. Similarly, hub nodes were classified as ‘provincial’ ($B_T < 0.3$), ‘connector’ ($0.3 \leq B_T < 0.8$) or ‘kinless’ ($P_i \geq 0.8$) hubs according to their relative participation in communication between modules (see Figure 1). The proportion of time spent as each of these cartographic classes was calculated for the resting state and stationary null datasets (Figures 2 and S3; images available at <http://neurovault.org/collections/HAWDIOCD/>; code for this experiment is freely available at <https://github.com/macshine/integration/>). To estimate the extent of each time-averaged system involvement in the different cartographic classes, we

calculated the percentage of each region type associated with each of 15 putative networks, based on an *a priori* classification from a separate study (35).

To determine whether there were distinct patterns of connectivity associated with each cartographic class, we calculated the frequency with which each of the 375 regions was present in the same temporal module as a region designated as either a connector or provincial hub. This allowed us to track the regions integrated by each hub over time (Fig 2).

Dynamic Fluctuations in Cartography

To track changes in brain-wide cartography over time, we calculated the total number of regions that were associated with each cartographic class within each temporal window. We then correlated the total number of regions residing in each class across all temporal windows using a Spearman's rho correlation. A Louvain clustering algorithm was utilized on the resultant correlation matrix and identified the presence of two main cartographic 'temporal clusters'. By calculating the sum of the number of regions associated with the cartographic classes within each 'state', we were able to track fluctuations in the states over time (Figure 3c). Given the predominance of peripheral nodes in the resting data, each state time series was standardized, which then allowed for the identification of temporal windows associated with either a segregated (i.e. greater relative number of uPN and PH; Z_s) or integrated state (greater relative number of PN, CN and CH; Z_i). The original 3D connectivity matrix containing MTD values was then reorganized into those windows associated with the two states (i.e. either Z_s or $Z_i \geq 1.65$). The modularity of each window was then calculated using the Louvain algorithm (Equation 2) and the resultant values were then compared statistically using an independent samples t-test (given the higher frequency of

the integrated state, a random sub-sample of these windows were selected to match the frequency of the segregated state). A similar technique was used to estimate the global efficiency of each temporal window. As global efficiency (Equation 5) cannot be computed from networks with negative weights (39), we first thresholded the connectivity matrix within each window at 5% density and then binarized the resultant matrix before calculating global efficiency.

$$E_{glob} = \frac{2}{n(n-1)} \sum_{i < j \in G} \frac{1}{d(i,j)} \quad [5]$$

Equation 4 – global efficiency of a network, where n denotes the total nodes in the network and $d(i,j)$ denotes the shortest path between a node i and neighboring node j .

Cartographic Profiling

To confirm that the discovery of the two temporal clusters was not biased by the specific choices of boundaries between cartographic classes, we performed clustering of temporal windows without the use of class labels. To do so, we classified the joint histogram of each temporal window (which is naïve to cartographic boundaries) over time using a k-means clustering analysis ($k = 2$; which was explicitly chosen in an attempt to replicate the finding of two states in the previous analysis; Z_I and $Z_S > 0$). As a result of this analysis, each window was assigned to one of two clusters. The presented results are from k-means with 500 random restarts (i.e. replicates as implemented in the MATLAB k-means function) to mitigate the well known sensitivity of k-means to initial conditions. We then compared the consensus partition of the joint histogram time series between the two methods. Consensus partitioning for joint histograms was created by calculating the percentage of time that two time points were in the

same module and then clustering the resultant matrix using the Louvain algorithm (39). The mean Dice's coefficient across 100 subjects was 0.792 ± 0.04 (Figure 3f). To compare this result to an appropriate null dataset, we created 2500 randomized binary vectors with the same mean as each subjects' data and then calculated the Dice's coefficient between these random vectors and the k-means results. The mean Dice's coefficient for this null dataset was 0.554 ± 0.08 , and as the mean Dice's coefficient for the clustering comparison was greater than the 95th centile of the null dataset, we were able to reject the null hypothesis that the observed Dice coefficient between clustering partitions was due to chance alone (38).

To ensure that the *a priori* choice of two clusters for the k-means analysis was reflective of the broader patterns in the data across multiple values of k , we re-ran the clustering analysis in the discovery cohort of 92 subjects across a range of k (2-20) and then compared the resultant cluster partitions to the original states identified using the Z_s and Z_I scores by calculating the mutual information between the each pair of partitions. The partition identified at each value of k was strongly similar to the pattern identified at $k = 2$ (mean mutual information = 0.400 ± 0.02). In keeping with the fact that we found strongly reproducible results for $k = 2$ across replication cohorts, this suggests that our choice of utilizing $k = 2$ to cluster the joint histograms over time was reflective of a "natural" clustering pattern in the data.

To estimate the patterns of brain connectivity associated with each state, we created a binary regressor for each subject that denoted windows associated with either the segregated ($Z_s > 1.65$) or integrated state ($Z_I > 1.65$). We then calculated a point-biserial correlation of each region-by-region connectivity measure and

the vector representing state identity. Resultant Pearson's correlation coefficients were then normalized using a Fisher's r-to-Z transform and compared between the two states using a paired-samples t-test (FDR, $p < 0.05$). The pairs of regions that survived correction were then reorganized according to a pre-defined network identity vector (35) and projected onto 375 x 375 adjacency matrix (see Figure S4).

Task-based Alterations in Cartographic Profile

To assess task-based functional connectivity, preprocessed data from the original 92 unrelated subjects from the discovery cohort were collected while these subjects performed two different tasks in the fMRI environment (31): i) a simple motor task in which the participants were presented with visual cues that required them to tap their left or right fingers, squeeze their left or right toes, or move their tongue in 2 x 12 second blocks of movement; and ii) a visually-based N-back task, which consisted of interleaved 10 second blocks of a high (2-back) and low (0-back) load N-back task, with object stimuli from four classes (places, faces, body parts and tools) (see (22) for further details of each experimental paradigm). Preprocessing of time series data involved distortion correction and linear head movement correction. The mean time series was then extracted from the same 375 regions as defined in the resting state analysis. To control for spurious patterns of connectivity associated with task-evoked activity, we first regressed the HRF-convolved task block data from each time series. The MTD metric was then calculated on the residuals of this regression using a window length of 14 (~10 seconds at 0.72 second TR). These data were then subjected to a cartographic profiling analysis in a similar fashion to the resting state data.

To compare the patterns of time-resolved connectivity across the two tasks to those observed during rest, the proportion of each task session associated with each cartographic class was compared to the proportion in both the other task and during rest using separate 1-way ANOVAs with post-hoc paired-sample t-tests (corrected for multiple comparisons using Bonferroni correction: $\alpha/5 = 0.01$). State Z-scores (Z_s = standardized sum of uPN + PH; Z_l = standardized sum of PN, CN & CH) were also calculated for each temporal window, and the proportion of TRs with a Z_s or Z_l score ≥ 1.65 with both task and rest blocks were calculated for each task.

We also tested whether any regions within the 2-dimensional space were significantly modulated by task by running a mixed-effects General Linear Model analysis at the individual level, fitting the group-averaged joint histogram to regressors tracking task and rest blocks in both the motor and the N-back task, separately. We then compared the two tasks > rest and the resting state data statistically using a two-sided one-sample t-test across subjects (FDR, $p < 0.05$). Finally, we estimated the relationship between task performance and modularity (Q) and efficiency (E) by calculating each topological measure over time during the task and then correlating the resultant vectors with convolved regressors that represented either task or rest blocks.

In order to assess the alteration in the cartographic profile as a function of task performance, we estimated the affine transformation (using a correlation cost function with 3 degrees of freedom, including translation and rotation parameters) between each individual subjects' resting state cartographic profile and the profile observed in both the motor and N-back task, separately. The transformation matrices were then entered into a random-effects analysis

comparing the movement of the cartographic profile as a function of task. Finally, to determine whether the cartographic profile dynamically reorganized as a function of task demands, we correlated the transformed resting state histogram (i.e. the resting state histogram 'shifted' according to the affine transform estimated in the previous step) with the histogram for each time point during each task, and the mean correlation for both the task and rest block regressors (trimmed of the first 11 time points to remove the effects of the previous block) for each subject. These values were then averaged (mean) across the cohort of 92 individuals.

Replication analysis

To quantify how well our results replicated across sessions and datasets, we calculated group-level correlations between each of the measures identified in our analysis. Overall, we observed a strong positive correlation between the outcome measures identified in the two sessions (for all statistical tests, $p < 0.0001$): graph measures – $r_{W_T} = 0.982$, $r_{B_T} = 0.957$ (see Figure S5); cartographic measures – $r_{uPN} = 0.973$; $r_{PN} = 0.974$; $r_{CN} = 0.853$; $r_{PH} = 0.903$; $r_{CH} = 0.730$; and temporal states (upper triangle of the state correlation matrices) – $r_{States} = 0.982$ (see Figure S6). We also confirmed the presence of these results in a unique cohort of 92 unrelated participants from the HCP: graph measures – $r_{W_T} = 0.971$, $r_{B_T} = 0.967$ (Figure S5); cartographic measures – $r_{uPN} = 0.962$; $r_{PN} = 0.960$; $r_{CN} = 0.918$; $r_{PH} = 0.921$; $r_{CH} = 0.755$; and temporal states – $r_{States} = 0.973$ (Figure S6).

We also observed similarly positive relationships between the group-level outcome measures estimated from the HCP and NKI data (for all statistical tests, $p < 0.0001$): graph measures – $r_{W_T} = 0.941$, $r_{B_T} = 0.857$ (Figure S5); cartographic

measures – $r_{uPN} = 0.923$; $r_{PN} = 0.830$; $r_{CN} = 0.771$; $r_{PH} = 0.767$; $r_{CH} = 0.564$; and temporal states – $r_{St \rightarrow tes} = 0.927$ (Figure S6). In addition, the mean joint histogram obtained from the NKI data was similar to the result observed in the HCP data (see Figure S7).

Validation analysis

Based on the novel methodology and short temporal windows utilized in this analysis, we performed numerous additional analyses to clarify the relationship between the main temporal outcome measures calculated in this study with respect to: i) the choice of functional connectivity algorithm; ii) the use of short windows; iii) the choice of high pass filter threshold; iv) the potential adverse effects of spurious noise during the resting state scanning session; and v) the choice of community detection algorithm.

Effect of connectivity algorithm

We have previously shown that the MTD is more sensitive and specific to subtle shifts in connectivity structure than those estimated using a sliding-window Pearson's correlation in simulated BOLD data (13). To determine whether using a sliding-window Pearson's correlation gave similar results to the MTD in this study, we re-analyzed the data in our experiment using a Pearson's correlation with a sliding window of $w = 14$ (the window length used in our experiment) and $w = 83$ (which equates to ~60 seconds, a commonly used window length in the neuroimaging literature) (41). While the estimates of W_T and B_T were similar between the two techniques (mean $r = 0.734$, $p < 0.001$), the cartographic profiling results were distinctly different, particularly with respect to the regions identified as hubs (mean Pearson's $r_{PH} = -0.021 \pm 0.02$; mean $r_{CH} = 0.017 \pm 0.01$), however the node estimate were similar between the two measures (mean $r_{uPN} =$

0.498 ± 0.04 ; mean $r_{PN} = 0.402 \pm 0.03$; mean $r_{CN} = 0.521 \pm 0.07$). Importantly, the results of the sliding window Pearson's analyses were less reproducible than the MTD across datasets at $w = 14$, with little or no correlation between hub structure across replication datasets ($r_{PH} = 0.034 \pm 0.05$; $r_{CH} = 0.019 \pm 0.07$).

Effect of window length

To determine the effects of using a short window length in the calculation of the MTD on the outcome measures in our experiment, we re-ran the analysis in all 92 subjects from the original group across a range of window lengths (10-100 in intervals of 5 TRs). We then compared the main outcomes measures in our study (parcel-wise mean W_T , mean B_T and percentage time as each cartographic class) across all window lengths in all 92 subjects using a region-wise Spearman's rho correlation (Figures S5 and S6). Although W_T , B_T and the percentage of time spent as a uPN, CN or PH were not affected by window length, there were observable differences in the estimates of the percentage of time spent as either an PN or CH using the MTD, suggesting that tracking patterns of connectivity at shorter windows (here, approximately 10 seconds) using the MTD affords a unique insight into spatiotemporal dynamics in fMRI BOLD data.

Effect of high pass filter threshold

Recent work on simulated time series has suggested that low frequency signals in fMRI BOLD data can spuriously effect estimates of sliding window covariance (41), and as such, it has been recommended that the lower bounds of the high pass filter used on BOLD data be set to the reciprocal of the window length used in the sliding window analysis (in our study, this would amount to a low pass filter of $\frac{1}{10.08}$ seconds ~ 0.1 Hz). In contrast, others have shown that using data

with a high signal to noise ratio can effectively mitigate the potential issues with aliasing (42). In addition, we have previously shown that the MTD is relatively insensitive to low frequency fluctuations (13), as the temporal differencing used to create the MTD renders the technique relatively insensitive to signals with a lower frequency than the upper bounds of the low pass filter. As such, in keeping with others (11), we chose to use a high pass filter of 0.071 Hz in our study. However, to explicitly test whether the inclusion of low frequency altered the outcome measures in our experiment, we re-ran our analysis over a range of high pass filters (0.001 to 0.1, in steps of 0.1), with a low pass filter of 0.125. Across this entire range, we did not observe any group-level differences in our outcome measures of interest (minimum $r = 0.718$, $p < 0.001$), confirming that the signals measured by the MTD were not adversely affected by spurious low frequency signals in the data.

Effect of preprocessing strategies

To determine whether head motion was associated with each measure, we calculated the first principal component of the 12 head motion parameters over time and then correlated this new vector with each outcome measure. We also correlated the framewise displacement as well as the DVARS values with each outcome measure. None of these correlations was significant at $p < 0.05$. To test for the effects of temporal ‘scrubbing’ (33) and global signal regression, we re-analyzed data for the original group of 92 subjects separately and then compared the outcomes measures across analyses. For the scrubbing analysis, time points associated with framewise displacement $> 0.5\text{mm}$ or DVARS $> 5\%$ were removed and missing data points were then imputed using linear interpolation. Using this technique, we observed strong positive correlations between outcomes measures across analyses (mean Pearson’s $r > 0.700$ for all comparisons), suggesting that

neither preprocessing strategy had a major effect on topological or topographic measures calculated using the MTD. Finally, to determine whether physiological sources of noise were associated with each measure, we convolved the heart rate and respiratory signals with a pre-defined transfer function (Chang and Glover, 2009) and then correlated the resultant vector either each outcome measure for the 92 subjects from the discovery group. In both instances, we did not observe a significant correlation between the outcomes of interest in our analysis and physiological signals (for each comparison, $r < |0.050|$, $p > 0.05$).

Effect of community detection algorithm

To ensure that the modularity assignment within each window was robust across community detection algorithms, we repeated the analysis using the Infomap algorithm (43) in the discovery cohort and observed broadly consistent results (mean mutual information between community partitions = 0.342 ± 0.16). Furthermore, we also used another popular method, multi-slice community detection (44), to detect community structure in the time-resolved brain. The temporal modules identified by this method (using standard parameters: $\gamma = \omega = 1$) also gave similar results (mean mutual information between community partitions = 0.447 ± 0.21). However, due to practical concerns regarding computational load and the fact that the Infomap algorithm requires the thresholding of an adjacency matrix (and as such, is insensitive to anti-correlations), we did not use either method for the full study.

Supplementary Figure Legends:

Figure S1: Experimental Design: time series data from 375 brain regions were extracted from 100 unrelated young adults (made available by the Human Connectome Project) and subjected to time-resolved connectivity analysis. After preprocessing, time-resolved functional connectivity was estimated using the Multiplication of Temporal Derivatives, which resulted in a weighted adjacency matrix for each temporal window. Community structure was computed within each temporal window, enabling the calculation of time-resolved module-degree Z-score (W_T) and participation coefficient (B_T). These values were then subjected to cartographic analysis of time-resolved functional connectivity. To test our results against the null model of stationarity, the covariance matrix from the resting state data was used to create 2500 unique null datasets using a Vector Autoregressive Model (denoted with subscript, VAR — i.e. W_{VAR} and B_{VAR}). This data was then subjected to an identical analysis pipeline, with the maximum statistic from each iteration extracted to populate a null distribution, against which results from the resting state data were compared for hypothesis testing.

Figure S2: Within- and Between-module connectivity: a) mean within-module connectivity calculated using the module-degree Z-score, W_T , within each temporal window (*Equation 3: Supplementary Materials*); b) between-module connectivity was computed using the participation coefficient, B_T (*Equation 4: Supplementary Materials*); c) individual resting state communities, pre-defined using the InfoMap community-detection algorithm (35), were differentially balanced towards either high time-resolved intra- (blue) or inter-modular connectivity (red); d) we observed an inverse correlation between mean W_T and

mean B_T across all 100 subjects ($r = -0.354$, $p < 0.001$) that was not present in the VAR null data ($r = 0.898$, $p < 0.001$).

Figure S3: Spatial topography associated with each class of node identified in the cartographic analysis: a) ultra-peripheral nodes – $B_T < 0.05$; b) Peripheral nodes – $0.05 \leq B_T < 0.3$; c) Connector nodes – $0.3 \leq B_T < 0.65$. Color intensity reflects the standardized percentage of time each region spent within each cartographic class. Key: uPN – ultra-peripheral nodes; PN – peripheral nodes; CN – connector nodes; PH – peripheral hubs and CH – connector hubs.

Figure S4: Regional connectivity differences between states: a) Significant differences in the mean connectivity matrix between the two States are plotted in yellow/red (Integrated State) and blue (Segregated State). Only results that survived correction after an independent-samples t-test with FDR 0.05 correction for multiple comparisons are shown; b) rows and columns reflect each of the 375 brain regions, organized according to clustering approach outlined in Gordon et al., 2014.

Figure S5: Replication of Within- and Between-module connectivity scores: spatial projection of W_T and B_T scores for the left hemisphere, subcortical and cerebellar regions for all subjects from each of the four samples used in the study.

Figure S6: Replication of States: correlation matrix for the sum of each class of cartographic region over time across all four samples used in the study, as well as the VAR null model, which was qualitatively distinct from the other four matrices.

Figure S7: Replication of Cartographic Profiles: mean joint histograms for single subject from each of the four samples using in the study, comparing the distribution of W_T and B_T values over each temporal window.

Figure S8: Effect of Window Length on Within- and Between-module connectivity: correlation matrices displaying the similarity of the average estimate of within- and between-module connectivity for the discovery cohort ($n = 92$) using a range of window lengths (5 – 100, in steps of 5).

Figure S9: Effect of Window Length on Cartographic measures: correlation matrices displaying the similarity of the percentage of time that each region spent as a given cartographic class. While the estimates for uPN, CN and PH were similar across all window lengths > 5 , there were marked differences in the regions identified as PN or CH at low to intermediate window lengths.

Figure S10: Temporal fluctuations in integration and segregation in the resting state: movie of a cartographic profile of resting state data from a single subject from the HCP dataset (subject #100307).

Figure S11: Temporal fluctuations in integration and segregation in the resting state: movie of a cartographic profile of resting state data from a single subject from the NKI Rockland dataset (subject #0102157).

Figure S12: Temporal fluctuations in integration and segregation during task performance: movie of a cartographic profile of N-back data from a single subject from the HCP dataset (subject #100307). A bar chart detailing the current block of the experiment is projected next to the cartographic profile.

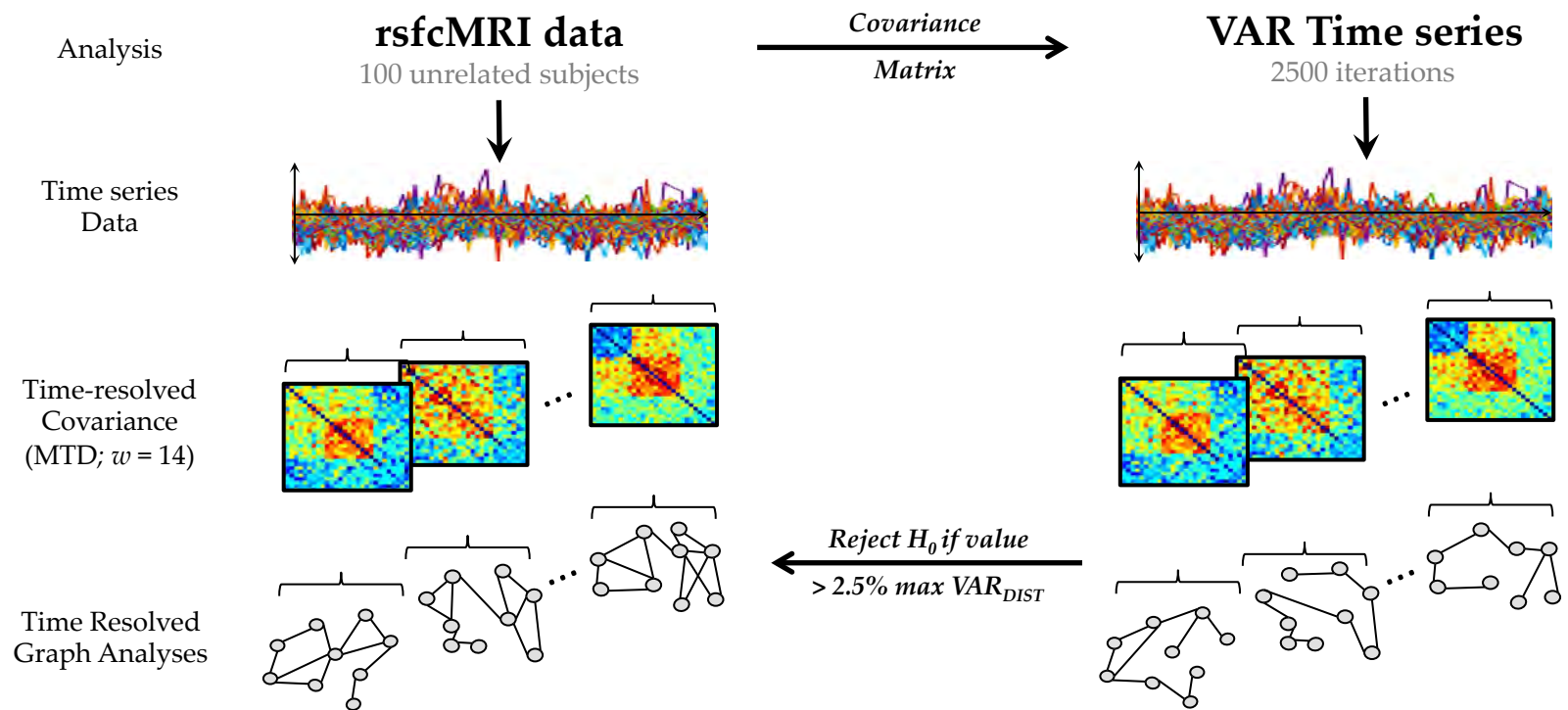


Figure S1

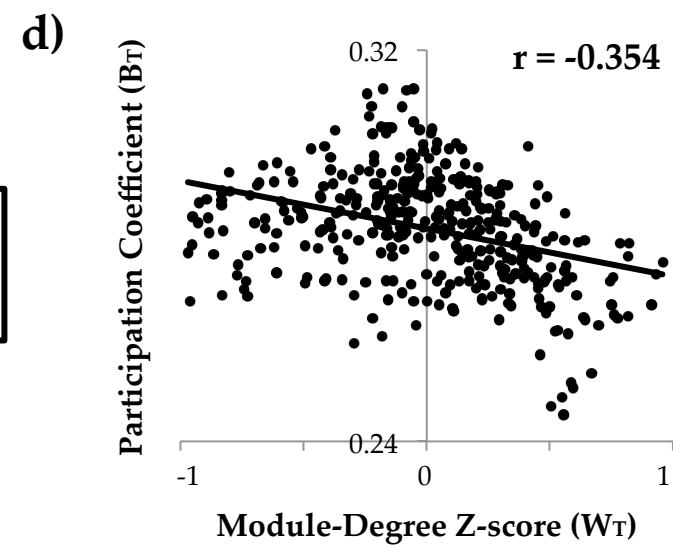
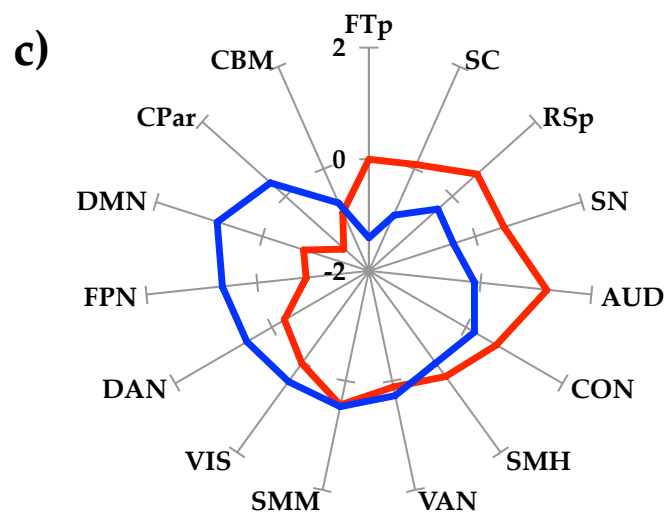
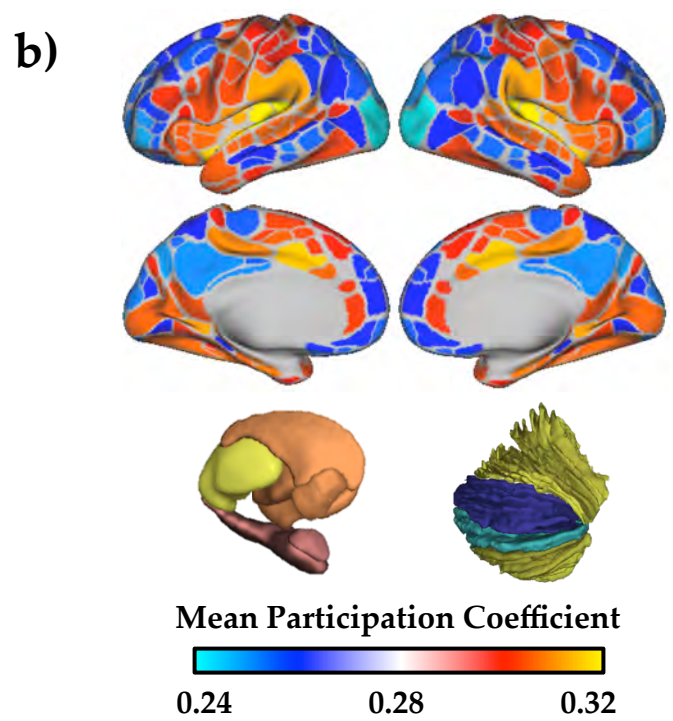
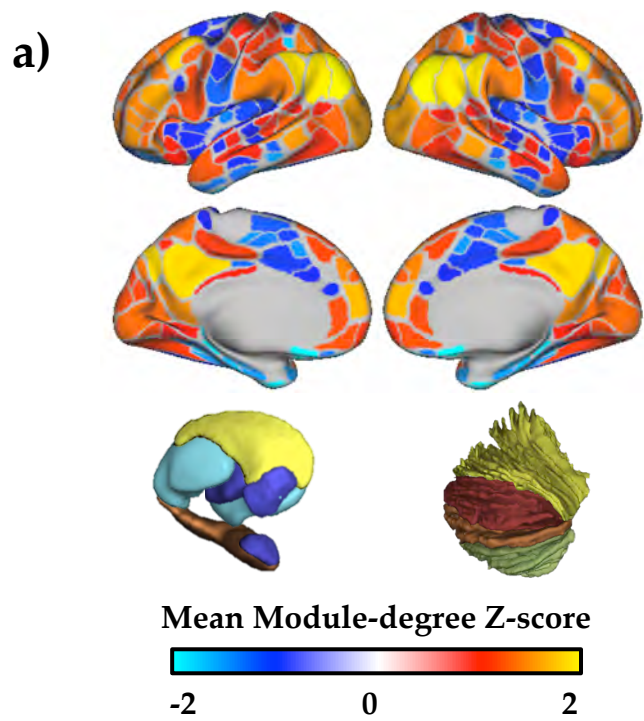
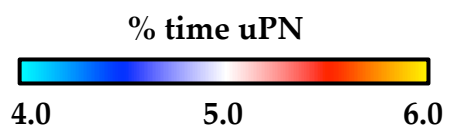
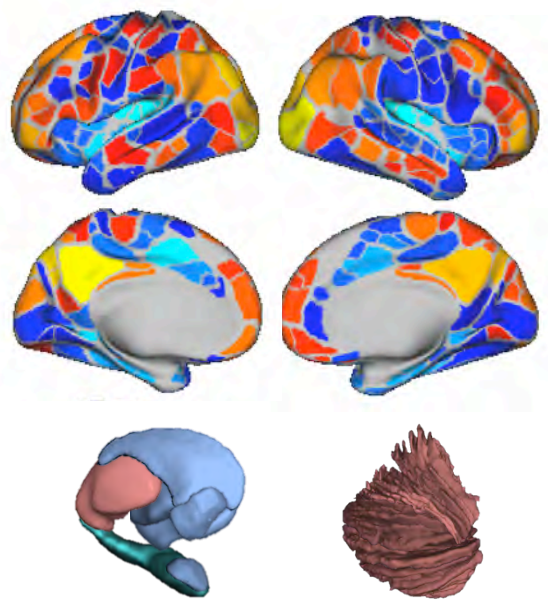
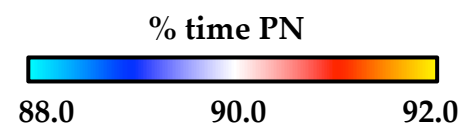
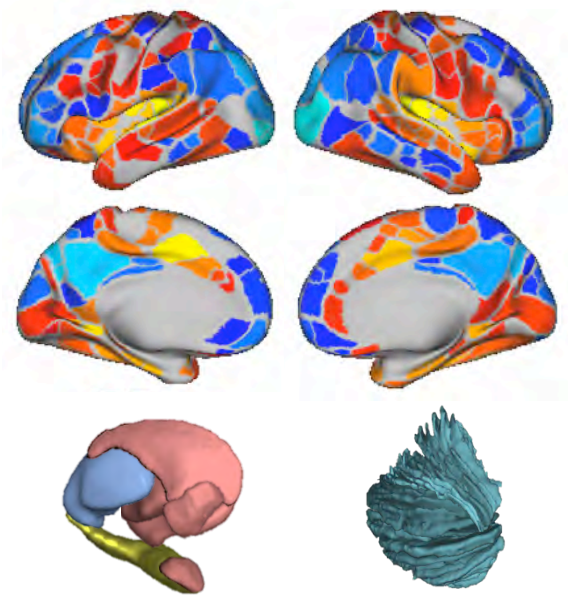


Figure S2

a) Ultra-Peripheral Nodes



b) Peripheral Nodes



c) Connector Nodes

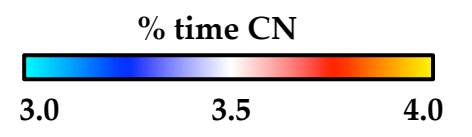
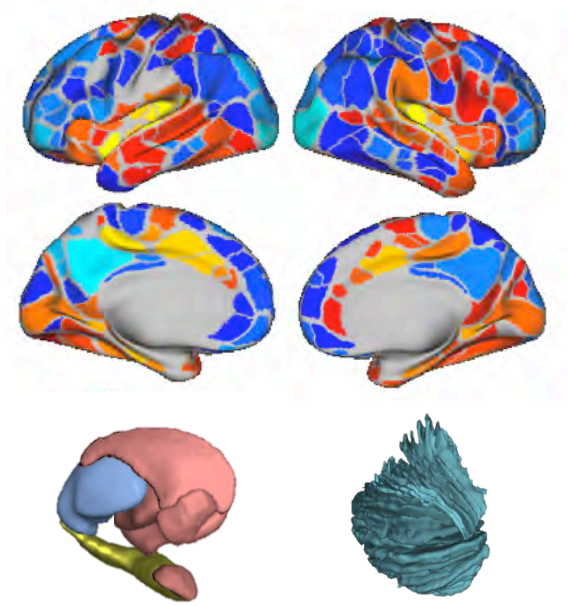
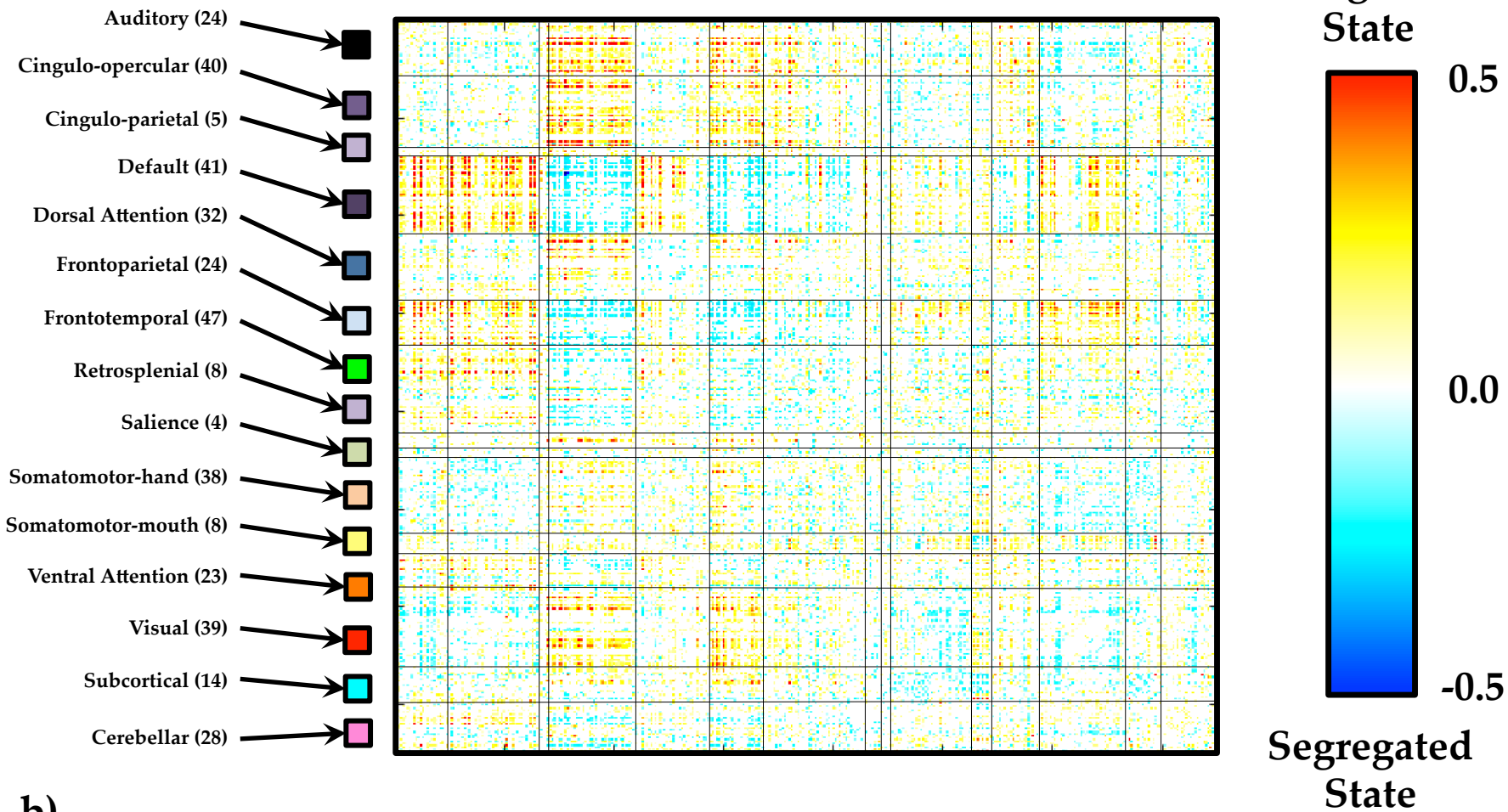


Figure S3

a)



b)

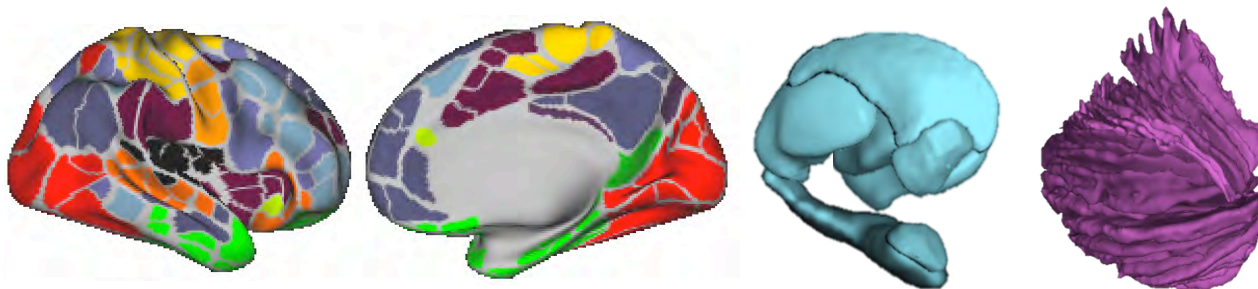
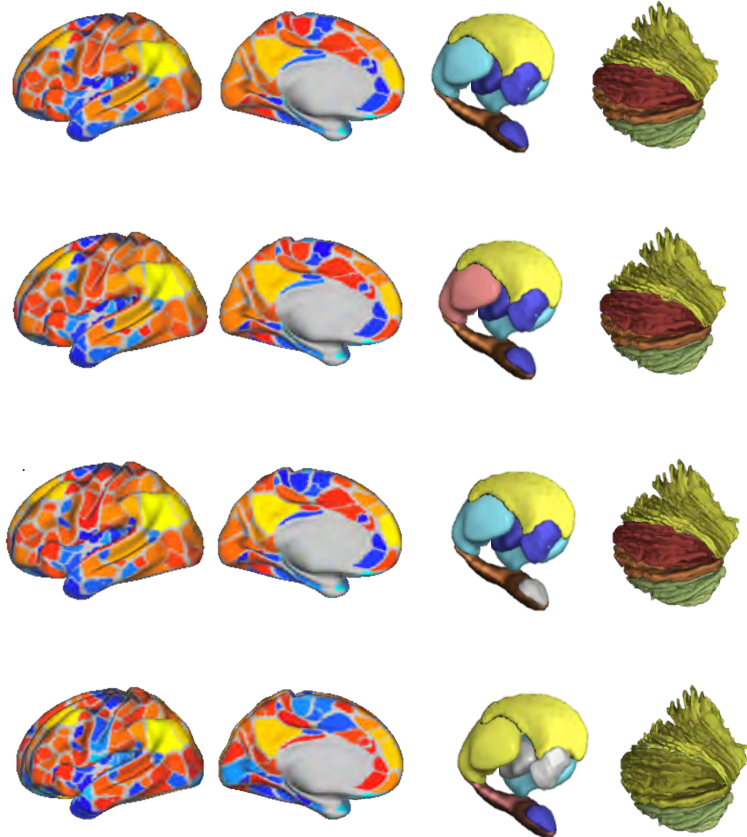


Figure S4

Replication Results

Within Module

Between Module

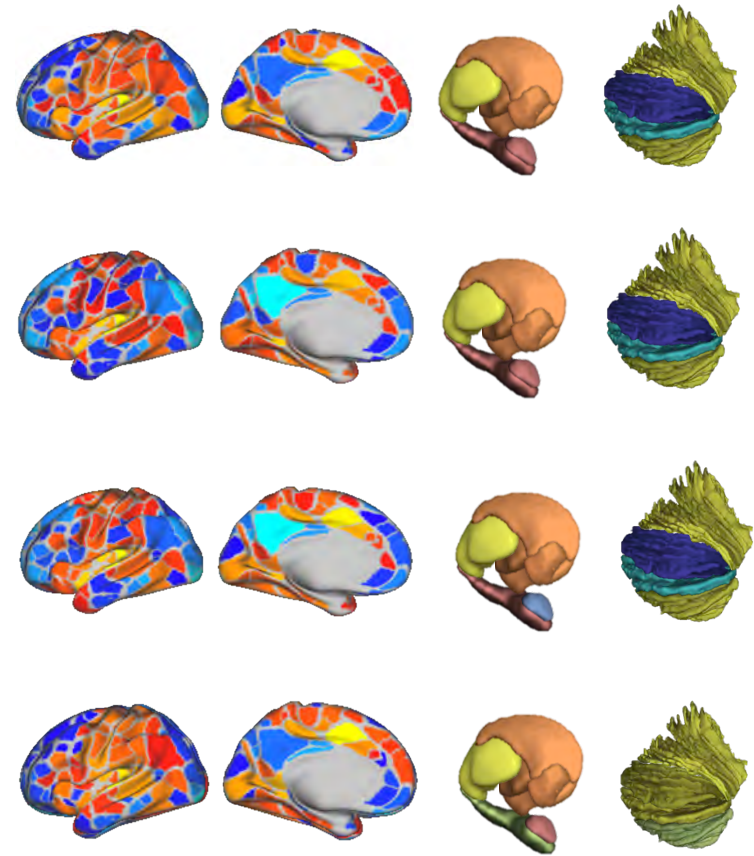


Original

Sessions

Subjects

Studies



Mean Module-degree Z-score



-2 0 2

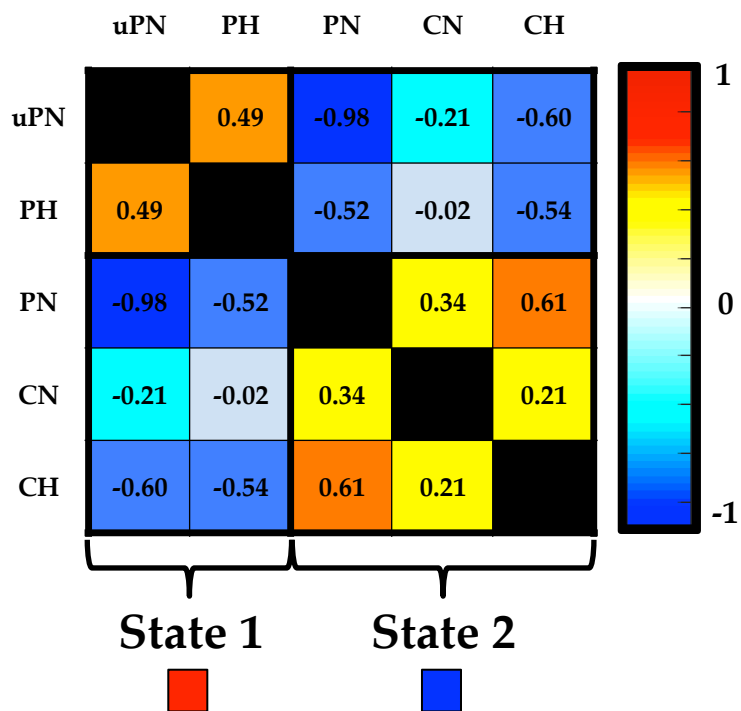
Mean Participation Coefficient



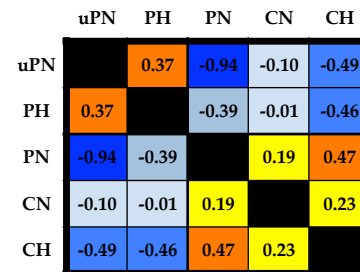
0.24 0.28 0.32

Figure S5

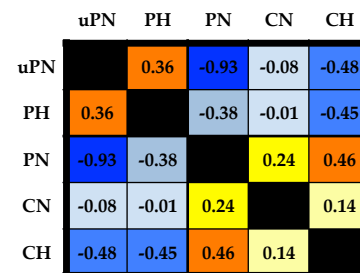
Original Data



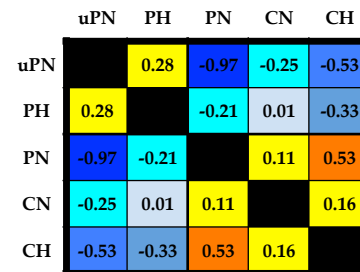
Across Sessions



Across Subjects



Across Studies



VAR null model

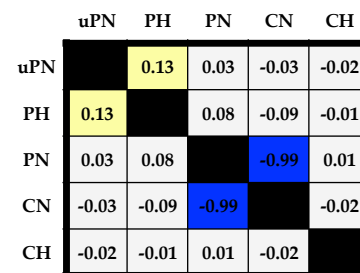
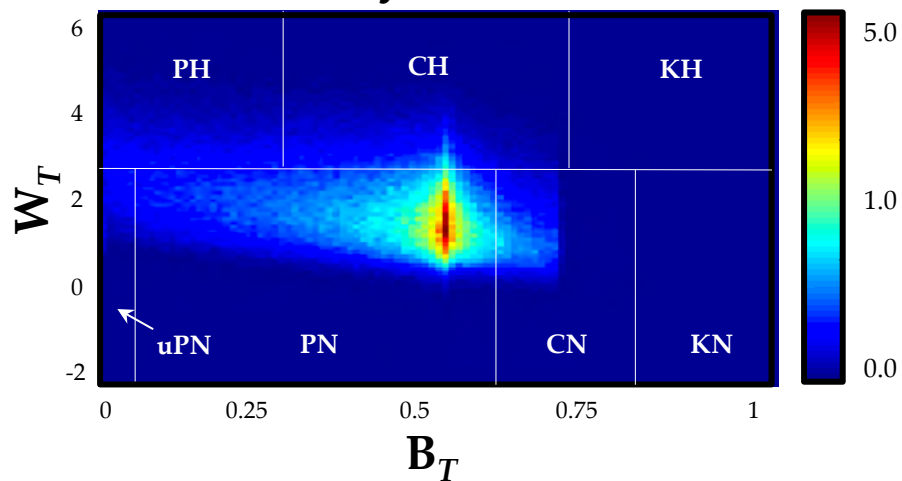
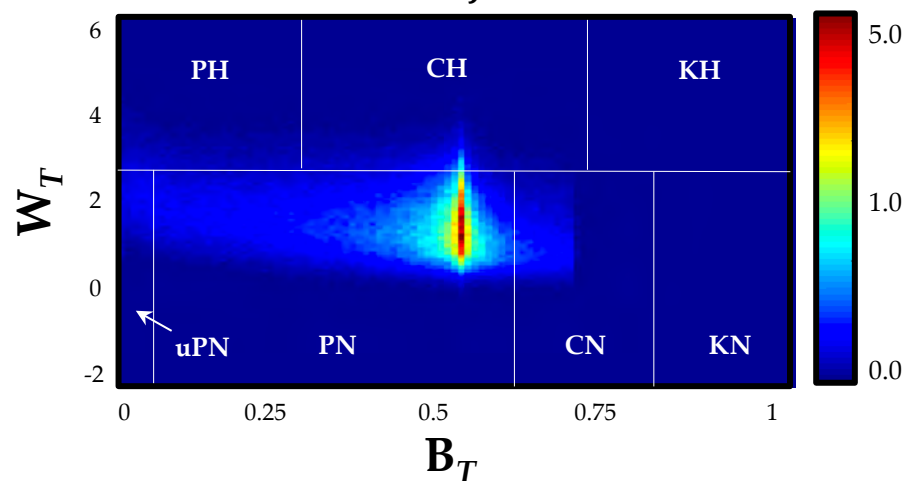


Figure S6

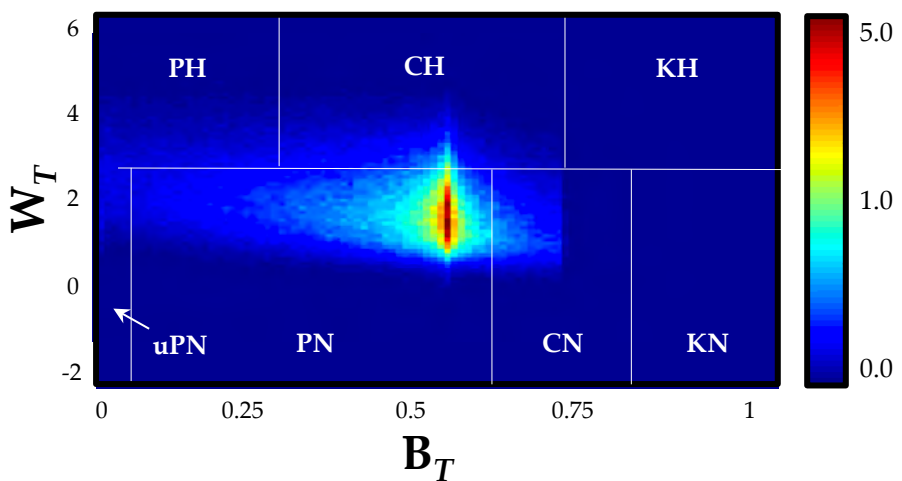
Discovery Cohort (HCP)



Across Subject (HCP)



Across Session (HCP)



Across Study (NKI)

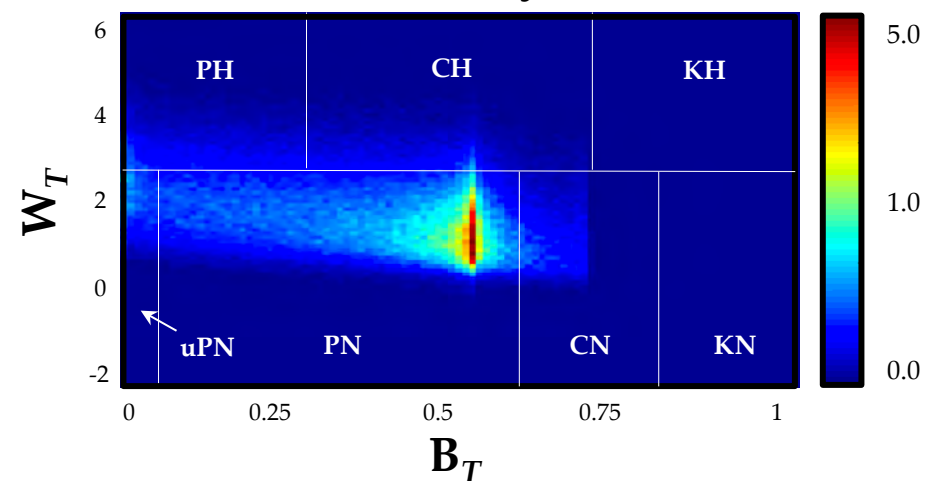


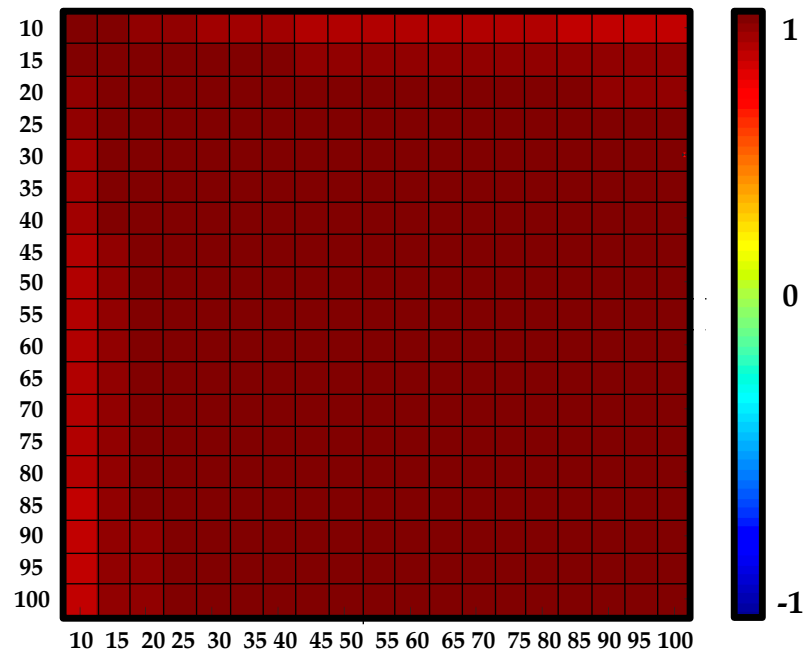
Figure S7

Effect of Window Length

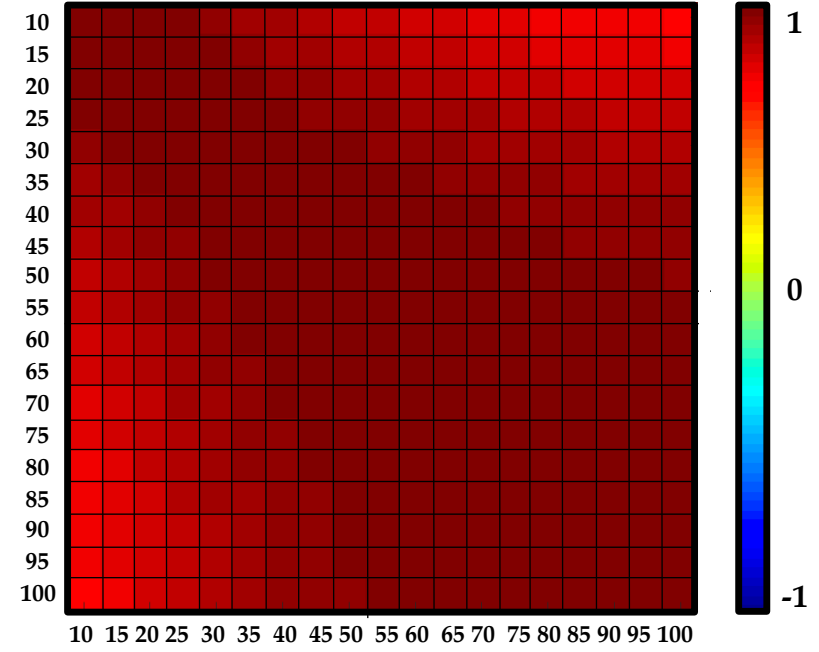
Within- and Between-Module Connectivity

W_T

B_T



Window Length (in TRs)

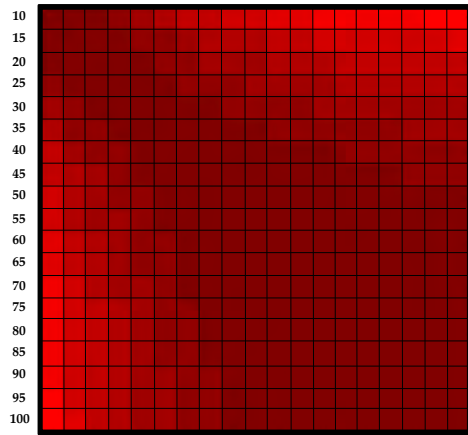


Window Length (in TRs)

Effect of Window Length

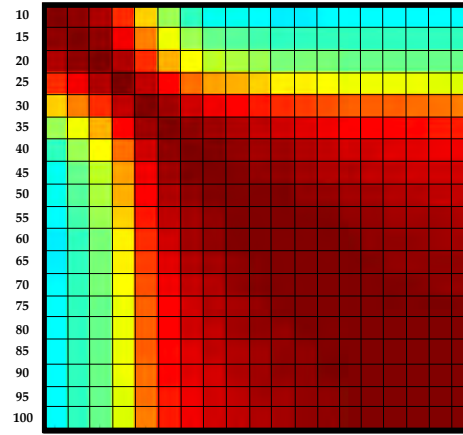
Cartographic Classes

uPN



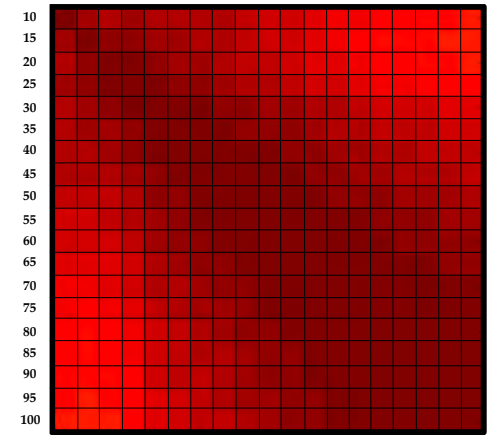
Window Length (in TRs)

PN



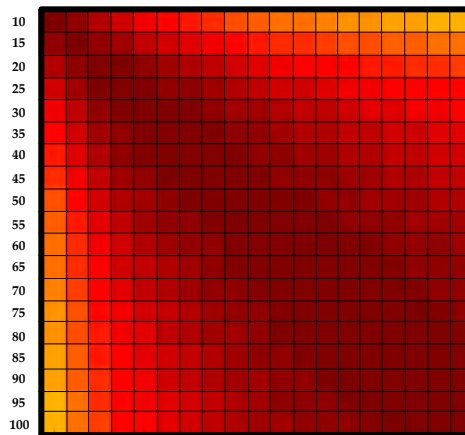
Window Length (in TRs)

CN



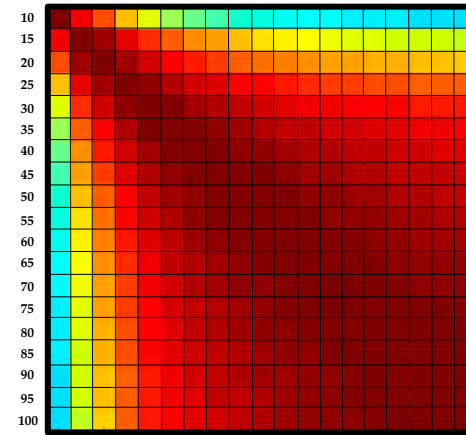
Window Length (in TRs)

PH



Window Length (in TRs)

CH



Window Length (in TRs)

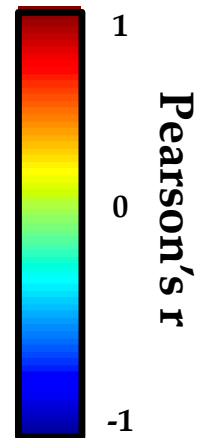


Figure S9